Simulation of Damage for Wind Turbine Blades Due to Airborne Particles

Giovanni Fiore[1] and Michael S. Selig[2]*
[1]Ph.D. Candidate, Department of Aerospace Engineering, University of Illinois at Urbana-Champaign, Urbana, Illinois 61801, USA, Email: gfiore@illinois.edu
[2]Associate Professor, Department of Aerospace Engineering, University of Illinois at Urbana-Champaign, Urbana, Illinois 61801, USA, Email: m-selig@illinois.edu

ABSTRACT

A mathematical model and simulation of airborne particle collisions with a 38 m, 1.5 MW horizontal axis wind turbine blade are presented. Two types of particles were analyzed, namely insects and sand grains. Computations were performed using a two-dimensional inviscid flowfield solver coupled with a particle position code. Three locations along the blade were considered and characterized by airfoils of the DU series. The insect simulations estimated the residual debris thickness on the blade, while sand simulations computed the surface erosion rate. Results show that the impact locations along the blade depend on angle of attack, freestream velocity, airfoil shape, and particle mass. Particles were found to collide primarily at the leading edge. The volume of insect debris per unit span was maximum at $r/R = 0.75$. The erosion rate due to sand was maximum on the low pressure side of the blade. An erosion rate approximately ten times higher was observed at $r/R = 0.75$, as compared with the section at $r/R = 0.35$. Near the leading edge, large angles of impact occurred and erosion rate had a minimum, while it reached maximum values slightly downstream where the impact angle was more skewed.

NOMENCLATURE

A	=	particle reference area	r/R	=	airfoil radial location on blade
AK	=	particle nondimensional mass	R_I	=	impact surface ratio
c	=	airfoil chord length	R_R	=	rupture surface ratio
COE	=	Cost of Energy	Re	=	particle Reynolds number
C_d	=	airfoil drag coefficient	Re_∞	=	freestream Reynolds number
C_D	=	particle drag coefficient	s	=	impact location along airfoil arc length
C_l	=	airfoil lift coefficient			
d	=	particle diameter	s_{tot}	=	airfoil total arc length
D	=	particle drag force	t	=	time
E	=	erosion rate	t/c	=	airfoil thickness-to-chord ratio
E_I	=	particle impact efficiency	U	=	chordwise velocity component
E_R	=	insect rupture efficiency	V	=	chord-normal velocity component
f	=	sand grain shape factor			
$GAEP$	=	Gross Annual Energy Production	V_∞	=	freestream velocity
h	=	airfoil projected height perpendicular to freestream	V_{imp}	=	particle impact velocity
			V_N	=	particle normal impact velocity
K	=	erosion rate constant	V_r	=	particle relative velocity
l	=	particle length	V_{rup}	=	insect rupture velocity
m	=	particle mass	x	=	particle x-location
n	=	erosion rate velocity exponent	y	=	particle y-location
Q	=	quantity of insect debris	α	=	angle of attack

*Corresponding Author: E-mail address: m-selig@illinois.edu.

α_r	=	relative angle between the	*Subscripts and superscripts*		
		flowfield and particle velocity	0	=	initial state
β	=	impingement efficiency	l	=	lower limit
ε	=	excrescence height	I	=	insect
η_R	=	insect rupture ratio	P	=	particle
λ	=	tip-speed ratio	r	=	relative
θ	=	impact angle	S	=	sand
μ	=	dynamic viscosity	u	=	upper limit
ρ	=	density			
τ	=	nondimensional time			

1. INTRODUCTION

Horizontal axis wind turbines (HAWTs) used for eletrical power generation are subject to fouling and damage by airborne particles associated with the environment in which wind turbines operate. Throughout the 20-year lifespan of a wind turbine, particles such as raindrops, sand grains, ice crystals, hailstones, and insects are major contributors to a deterioration in turbine performance through local airfoil surface alterations [1–4]. Turbine blades accumulate dirt especially in the surroundings of the leading edge. Moreover, particle collisions, temperature jumps and freeze-thaw cycles may cause existing cracks in the coating to propagate, promoting coating erosion, core delamination, and corrosion damage due to exposure of the internal composite structure. The originally smooth surface of the blades may change considerably, and in such cases the increased roughness will cause a reduction in power output. For instance, once an insect collides and adheres to the surface of the blade, the boundary layer is adversely affected and local flow separation may occur if the residual debris thickness is comparable to the boundary layer critical height [5, 6]. However, even when this situation is seemingly minor, the drag coefficient is still increased due to boundary layer early transition [7]. When substantial insect fouling occurs, the critical roughness height is easily reached in the proximity of the blade leading edge. In such conditions, a bimodal electrical power output behavior was observed for stall-regulated HAWTs [8]. Reductions of the nominal power output up to 25% were reported during high wind days for this type of turbine [9].

New advancements in wind resource assessment have shown the benefits of offshore megawatt-scale wind turbine installations [10, 11], in order to maximize GAEP while reducing COE. However, offshore locations are subject to more intense sand erosion than the majority of land installations [12–14]. Airborne sand particles collide with the blade and cause microcutting and plowing in the coating material [15, 16] resulting in surface abrasion [17, 18]. Such damage is particularly prominent at the outboard sections of the blade where the local relative velocity is larger compared with inboard sections [12].

Wind farm operators are forced to schedule blade inspection and maintenance to reduce the cost of ineffective electric power production due to degraded wind turbine blades. Disassembling a wind turbine for factory inspection is costly, so the majority of servicing is performed on site. Damaged areas are located through blade visual inspection, surface alterations are smoothed through primer application and a protective polyurethane-based film is applied [19, 20]. However, because of the highly competitive nature of the wind turbine industry, the majority of wind turbine manufacturers are reluctant to share details of the construction materials with maintenance companies. Therefore, technical expertise plays a critical role in blade repair success and effectiveness [2, 21]. Moreover, repairs are mostly performed in the vicinity of the leading edge and not necessarily on all areas exposed to damage. Further downstream, blade areas eroded by sand and damaged by insect debris may be left untreated, promoting the enlargement of surface damage starting at coating weakened points. An estimated 6% of overall repairs and maintenance resources for wind turbines is dedicated to rotor blades [22, 23]. Moreover, an analysis of wind turbine reliability showed that tip break and blade damage are the first and third most common failure modes for wind turbines, respectively [23].

A few other detrimental aspects are involved with wind turbine operational damage. From an aerodynamic standpoint, a reduction in aerodynamic efficiency associated with an increase of the drag coefficient results from exposure to environmental airborne particles [24–26]. Also, an increasingly important issue associated with damaged blades is the level of noise generated. Blade surface alterations may increase the level of noise generated by perturbing the boundary layer

pattern [27]. From a technological stand-point, specialized surface coatings have been developed to assure a consistent aerodynamic performance and adequate structural integrity throughout the lifespan of a wind turbine [28]. Modern wind turbines are delivered with a factory-applied coating, and the majority of coating materials are polyurethane-based [29].

The goal of this study was to compute the trajectory of insects and sand grains and to characterize the impact areas of three sections along a wind turbine blade located at 35%, 65% and 75% of the span. A three-blade, 38 m radius, 1.5 MW HAWT was chosen as a baseline for the computations, being at present the most common wind turbine configuration in North America [30]. Two computational models were implemented to characterize the damage due to insect fouling and sand erosion, and these models are discussed. This paper is divided into five sections: the numerical method used for the computations is described in Section 2, the blade operating point, particle aerodynamics, and blade damage models are introduced in Section 3, the results obtained along with a proposed operational damage model are discussed in Section 4, and finally, conclusions are presented in Section 5.

2. METHODOLOGY AND THEORETICAL DEVELOPMENT

Predicting the trajectory of impinging particles is critical when impact characteristics on the wind turbine blade need to be determined. A lagrangian formulation code was developed in-house and named BugFoil. BugFoil integrates a pre-existing insect trajectory code [31] and a customized version of XFOIL [32]. Local flowfield velocity components are obtained by querying the potential flow routine built in XFOIL, from which the particle trajectory and impact location on the airfoil are computed. Similarly, the capabilities of BugFoil have been expanded to simulate trajectories of sand grains.

In steady flight, the forces acting on the particle are perfectly balanced. Perturbations to such forces are assumed to be additive to the steady-state forces. For these reasons the equations of motion may be expressed by neglecting the steady-state forces and may be written as functions of increments only [33]. In the current study, both insects and sand grains were treated as aerodynamic bodies whose only associated force is the aerodynamic drag D. The main advantage of this assumption was to simplify the evaluation of insect trajectory because the effects of lift due to the wings are considered to be negligible compared with drag and inertia forces. It should be noted here that regardless of the insect and blade relative orientation during impact, the chosen approach allowed for trajectory evaluation. On the other hand, considering the insect lift force would pose the issue of estimating the direction and magnitude of such force in a two-dimensional plane throughout the entire rotating envelope of the wind turbine blade.

By applying Newton's second law along the particle trajectory in both chordwise x and chord-normal y directions, the following equations are obtained [15, 34–36]

$$m_p \frac{d^2 x_p}{dt^2} = \sum F_x \tag{1}$$

$$m_p \frac{d^2 y_p}{dt^2} = \sum F_y \tag{2}$$

By projecting the drag of the particle D in both chordwise x and chord-normal y directions using the relative angle between particle and flowfield velocity α_r, the equations may be rewritten as

$$m_p \frac{d^2 x_p}{dt^2} = \Delta D \cos \alpha_r \tag{3}$$

$$m_p \frac{d^2 y_p}{dt^2} = \Delta D \sin \alpha_r \tag{4}$$

Given the particle velocity components U_P and V_P and given the velocity flowfield components U and V at a certain point along the trajectory, the relative particle velocity V_r can be expressed as

$$V_r = \sqrt{(U - U_p)^2 + (V - V_p)^2} \tag{5}$$

while the trigonometric functions in Eqs. (3) and (4) may assume the form

$$\cos\alpha_r = \frac{U - U_p}{V_r} = \frac{V_{rx}}{V_r} \qquad (6)$$

$$\sin\alpha_r = \frac{V - V_p}{V_r} = \frac{V_{ry}}{V_r} \qquad (7)$$

By expressing the particle aerodynamic drag D as a function of dynamic pressure and by substituting for the trigonometric functions, Eqs. (3) and (4) may be rewritten as

$$m_p \frac{d^2 x_p}{dt^2} = \frac{1}{2}\rho V_r^2 A_p C_D \frac{V_{rx}}{V_r} \qquad (8)$$

$$m_p \frac{d^2 y_p}{dt^2} = \frac{1}{2}\rho V_r^2 A_p C_D \frac{V_{ry}}{V_r} \qquad (9)$$

To scale this problem in a non-dimensional fashion, non-dimensional time, space, and mass parameters can be introduced as

$$\tau = \frac{tU}{c} \qquad (10)$$

$$\bar{x}_p = \frac{x_p}{c} \qquad (11)$$

$$\bar{y}_p = \frac{y_p}{c} \qquad (12)$$

$$AK = \frac{2 m_p}{\rho A_p c} \qquad (13)$$

Nondimensionalization of Eqs. (8) and (9) by the reference velocity U yields

$$\frac{d^2\bar{x}_p}{d\tau^2} = \frac{1}{AK}\bar{V}_r C_D \bar{V}_{rx} \qquad (14)$$

$$\frac{d^2\bar{y}_p}{d\tau^2} = \frac{1}{AK}\bar{V}_r C_D \bar{V}_{ry} \qquad (15)$$

which represents a set of second-order, nonlinear differential equations. Once the drag coefficient of the particle is evaluated, the trajectory can be computed by numerically solving both x and y equations.

3. BLADE DAMAGE ANALYSIS

The selected configuration is a three-blade, 1.5 MW, 38 m radius, $\lambda = 8.7$ wind turbine. Starting at the blade root and moving toward the tip, the airfoils used are the DU 97-W-300, DU 96-W-212, and DU 96-W-180. The airfoils relative thickness t/c and chord length c decrease along the blade span, in accordance to conventional wind turbine designs. A wind speed of 10.5 m/s at the hub height was selected for the chosen configuration [37]. The blade properties and inflow conditions are summarized in Table 1. Since modern wind turbines are operated close to their maximum lift-to-drag ratio [37, 38], the three sections of the blade were analyzed with XFOIL and three values of C_l were determined in the proximity of $(C_l/C_d)_{max}$. The operating conditions for the three blade sections are given in Table 2. Simulations for impact and damage due to insects and sand grains were performed at three angles of attack corresponding to the values of C_l determined.

3.1. Trajectory evaluation

BugFoil is initialized using nondimensional input data. An equally-spaced array of particles is placed five chord lengths upstream of the airfoil, with both initial velocity components nondimensionalized with respect to the local freestream velocity V_∞. Each particle is evaluated individually throughout its trajectory by numerically solving the particle equations of motion

Table 1. Baseline blade parameters

r/R	Airfoil	c (m)	V_∞ (m/s)	Re_∞
0.35	DU 97-W-300	3.13	33.70	7.26×10^6
0.65	DU 96-W-212	2.08	60.41	8.64×10^6
0.75	DU 96-W-180	1.73	69.44	8.25×10^6

Table 2. Blade section operating conditions

r/R	α (deg)	C_l	C_l / C_d
	3.5	0.83	101.81
0.35	5.5	1.09	126.52
	7.5	1.34	142.32
	4.0	0.81	151.87
0.65	6.0	1.04	151.07
	8.0	1.24	119.82
	4.0	0.79	167.62
0.75	6.0	1.02	172.54
	8.0	1.21	124.94

through a predictor-corrector algorithm. As the particle approaches the airfoil, the code verifies whether impingment occurs, and the impingement locations over the airfoil are determined. By taking the derivative of the initial particle coordinate y_0 with respect to the impingement location in arc lengths s, the impingement efficiency is defined in the following manner

$$\beta = \frac{dy^0}{ds} \tag{16}$$

The parameter β is also referred to as collection efficiency in other studies [34]. By computing the incoming trajectories for a vertical array of particles, the two outermost impacting ones correspond to $\beta = 0$. Those trajectories represent the upper and lower limits of impingement. The fraction of striking particles out of the total number is evaluated by localizing the initial upper and lower y-limits on the upstream array of particles, namely $y_I^{0,u}$ and $y_I^{0,l}$, as shown in Fig. 1. By dividing the distance between these two locations by the airfoil projected height h, the nondimensional impact efficiency parameter E_I is introduced as

$$E_I = \frac{y_I^{0,u} - y_I^{0,l}}{h} = \frac{\Delta y_I^0}{h} \tag{17}$$

The parameter E_I represents the height of the particle array captured by the airfoil, relative to the airfoil projected height.

When simulating the insect trajectories, impingement may transition to rupture depending on the impact velocity and bug species. Rupture is evaluated in the code by comparing the normal impact velocity V_N with the insect rupture velocity V_{rup}. A useful parameter, the rupture efficiency E_R, represents the fraction of impacting insects that ruptures. Rupture efficiency is modeled by locating the upper and lower rupture limits on the initial insect array (see Fig. 1) and is computed as

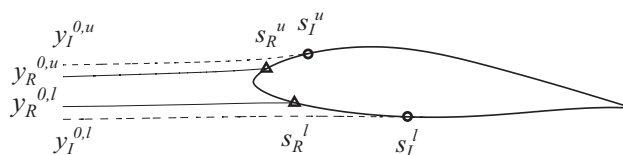$$\eta_R = \frac{E_R}{E_I} \tag{18}$$

Figure 1. Definition of particle impact and rupture limits.

A measure of the relative quantity of rupturing insects with respect to the impacting total is given η_R defined as follows

$$\eta_R = \frac{E_R}{E_I} \qquad (19)$$

The parameter η_R represents a figure of merit of the airfoil since it incorporates the rupturing mechanism of insects. An advantage of using η_R is being independent from the airfoil projected height h, which may not have a linear relationship with the angle of attack.

One way to estimate the blade surface area subject to particle collisions is to compute the airfoil arc length within the upper and lower surface impingement limits, s_I^u and s_I^l, respectively, as shown in Fig. 1. The result of this operation is called Δs_I. By knowing the total airfoil arc length s_{tot}, the impact surface ratio R_I can be computed as

$$R_I = \frac{s_I^u - s_I^l}{s_{tot}} = \frac{\Delta s_I}{s_{tot}} \qquad (20)$$

As R_I approaches unity, a larger portion of the blade area is subject to particle collision. In a similar manner, when considering the fouling due to insects, the rupture surface ratio R_R may be defined as

$$R_R = \frac{s_R^u - s_R^l}{s_{tot}} = \frac{\Delta s_R}{s_{tot}} \qquad (21)$$

The parameter R_R represents the amount of blade surface where rupture occurs.

3.2. Aerodynamics of the insect

Early studies on atmospheric insect population were performed to sample and identify flying insect species in the atmospheric region 100 m above the ground in southern Great Britain [39]. It was discovered that the most prominent species in those conditions were *aphids and drosophila melanogaster*, commonly known as the fruit fly. At present, however, entomology literature does not report extensive studies on insect population around the world and at various aerial heights. Later aerodynamic studies conducted on fruit flies were able to estimate lift and drag coefficients of the wings of such insects [40, 41] along with insect rupture velocity ($V_{rup} = 10.8$ m/s). Such information was used to simulate *drosophila head*-on impingement over wings of air-planes [31]. In the current study, however, the insect was considered to be steady in hovering flight, due to the large difference between the *drosophila* flying speed (≈ 2 m/s [42]) and the much higher blade local speed (see Table 1). Moreover, the lift contribution due to the wings was considered negligible when compared with inertia and drag forces of the body, as explained in Section 2.

The overall *drosophila* aerodynamic drag is dominated by viscous forces since its flight Reynolds number is typically $Re \approx 10^2$ [43–45]. The insect body drag coefficient can be approximated by the drag coefficient of spherical shapes in the same Reynolds number range [35, 46] and by fitting it to experimental drag values for *drosophila* [31, 40], that is

$$C_D = \frac{9.8}{Re}(1 + 1.97 \times 0.1 \ Re^{0.63} + 2.60 \times 0.0001 \ Re^{1.38}) \qquad (22)$$

where Re is based on insect body diameter. The reference value of *drosophila* body mass [31] is $m_I = 8.7 \times 10^{-4}$ g. The *drosophila* input data used for computing trajectories is summarized in Table 3. Note that V_{rup} is nondimensionalized by V_∞ at each blade section.

Table 3. Insect input parameters

r/R	Re	AK_I	l_I/c	V_{rup}/V_∞
0.35	1562.7	0.283	2.152×10^{-4}	0.322
0.65	2800.5	0.426	3.241×10^{-4}	0.180
0.75	3219.2	0.514	3.900×10^{-4}	0.156

3.3. Insect fouling

After impacting, insects leave streaks of fluids and fragments on the surface of the blade. The debris thickness, called here excrescence height ε, is numerically evaluated on the blade sections. Excrescence height is computed through normal impact velocity V_N as an interpolation of experimental impact data for *drosophilas* [5, 47]. The maximum excrescence height follows the nondimensional empirical law given by [31]

$$\left(\frac{\varepsilon}{l_I}\right)_{max} = 0.088165 \left(\frac{V_N}{V_{rup}}\right)^2 - 0.53289 \left(\frac{V_N}{V_{rup}}\right) + 1.3856 \tag{23}$$

where l_I is the insect body length (see Table 3). The normalized excrescence height ε/l_I as a function of β is given as

$$\left(\frac{\varepsilon}{l_I}\right) = c_0 + c_1\beta + c_2\beta^2 + c_3\beta^3 + c_4 \exp^{(c_5 \beta)} \tag{24}$$

where the coefficients c_i are obtained by fitting experimental debris height measurements. Integrating ε/l_I along the insect impingement limits over the airfoil yields the quantity of insect debris Q, that is

$$Q = \frac{1}{l_I} \int_{s_I^l}^{s_I^u} \varepsilon \, ds \tag{25}$$

The nondimensional parameter Q represents the volume of insect debris per unit span of the blade.

3.4 Aerodynamics of the sand grain

Airborne sand particles are mainly represented by silica-based grains. To incorporate shape irregularities typical of sand grains, the aerodynamic drag is modeled by means of a shape factor f defined as [46]

$$f = \frac{a}{A_s} \tag{26}$$

where a is the surface area of a sphere with the same volume of the sand grain, and A_S is the actual surface of the sand grain. Note that for perfectly spherical particles the shape factor is equal to unity. The drag coefficient for a sand grain is written in the form [46]

$$C_D = \frac{24}{Re_r} (1 + b_1 Re_r^{b_2}) + \frac{b_3}{1 + \dfrac{b_4}{Re_r}} \tag{27}$$

where the b_i coefficients are functions of f, and Re_r is the relative Reynolds number defined as

$$Re_R = \frac{\rho \, ds \, |Us - U|}{\mu} \tag{28}$$

The aerodynamic drag force can be expressed as [14, 36]

$$D = \frac{18\mu}{\rho_s d^2} \frac{C_D Re_r}{24} \tag{29}$$

The sand grain lift coefficient C_L is assumed to be negligible.

3.5. Sand erosion

Sand erosion has been investigated for a variety of air-breathing engines in aerospace applications [18, 36, 48, 49]. Sand grain velocities in the compressor stages are in the same range of the wind turbine erosion scenario. Erosion is responsible for an increase in blade surface roughness and a decrease in structural stiffness. The parameter erosion rate E, defined as the removed mass of the target

material divided by the mass of the impacting particle, is a function of particle impact velocity V_{imp} and angle at impact θ, and it is measured in (g/g) [16]. Impact velocity is related to E through a power-law; whereas, the correlation with impact angle strongly depends on the eroded material properties. Erosion is characterized by two contributions: a plastic and a brittle erosion mode [15, 16] that depend on the value of θ at which E is maximum. Most current materials used for wind blade coating are polyurethane derivatives [50] and show a primarily plastic erosion behavior with maximum erosion rate at $\theta = 30$ deg [51]. A common way to model the erosion rate for plastic materials is given by the equation [17, 49, 52–54]

$$E = K V_{imp}^{n} \tag{30}$$

where K and n are constants of the eroded material. The correlation between E and θ is implicit in the parameters K and n fitted at various impact angles and impact velocities.

Unfortunately, there exists a lack of experimental data on polyurethane erosion at various impact velocities [28]. At present, most of the experimental research on erosion is aimed at characterizing polyethylene-based coatings, which have a similar erosion behavior as compared with polyurethane [51]. For these reasons, the simulations were performed by using linear-fitted erosion constants of ultrahigh molecular weight polyethylene (UHMWPE) (see Table 4) because it has the best performance of the polyethylene-based coatings [52]. Silica octahedron-like grains typical of desert sand were considered for the simulation [46], with $f = 0.846$. A diameter of 200 μm was chosen to be representative of common sand grain size distributions. The sand data used to initialize the simulations is summarized in Table 5.

3.6. Code validation

The work by Bragg et al. [31] was used as a benchmark to validate the code implemented for this study, BugFoil. While BugFoil makes use of a subroutine based on fluid potential theory included in XFOIL [32, 55], the other work used a modified version of the Theodorsen method to obtain the flowfield velocity components around the air-foil. Two insects impingement conditions are simulated on a NACA 63A-415 airfoil, corresponding to $\alpha = -0.36$ and 3.0. A comparison of β-curves is shown in Fig. 2. A good agreement exists between the two methods. The trend and shape of the β-curves are well captured by BugFoil at both angles of attack. A slight shift of β peaks can be seen toward larger values of s. When using BugFoil, the maximum values of β appear exactly at $s = 0$ with insensitive behavior to a change in angle of attack. Moreover, the impingement limits are moved toward larger values of s at both angles of attack. It may be concluded that the airfoil circulation computed by the fluid potential method in BugFoil is slightly higher than the circulation obtained by the inviscid Theodorsen method. In fact, if the airfoil is assumed to be a lumped vortex of intensity equal to its circulation, the effect of an increased vorticity will move the impingement limits toward higher values of s and will move the β-peak to the right.

Table 4. Erosion constants

θ (deg)	K	n
0	0.0	2.8000
15	1.366×10^{-9}	2.8065
30	3.337×10^{-9}	2.6056
60	1.490×10^{-9}	2.6500
90	2.350×10^{-11}	2.6500

Table 5. Sand input parameters

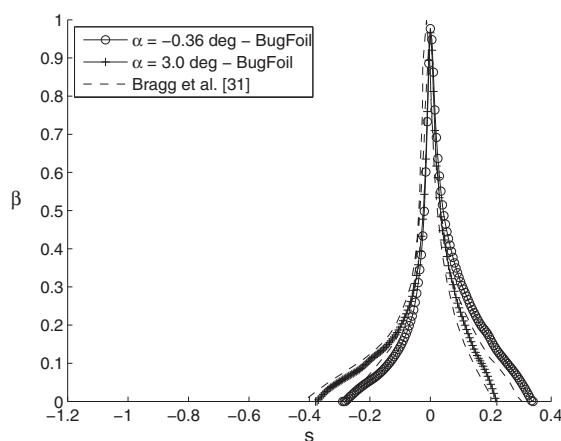| r/R	Re	AK_s	d_s/c
0.35	464.0	0.181	6.389×10^{-5}
0.65	831.5	0.272	9.624×10^{-5}
0.75	955.7	0.328	1.158×10^{-4}

Figure 2. Validation of BugFoil on a NACA 63A-415 airfoil – comparison of β-curves.

4. RESULTS AND DISCUSSION

All simulations were performed by initializing BugFoil with the input parameters for insect and sand grain reported in Tables 3 and 5 respectively. Each location along the blade span was analyzed at three operating points corresponding to three angles of attack as reported in Table 2. A single simulation required an average of 2 sec of computation time on an Intel Core i7 machine with 8 GB RAM running LinuxMint OS.

In order to characterize the particle impact locations along the airfoil, a useful measure is given by the airfoil arc length s. The parameter s is defined as the length of the arc starting at the particle impact location and ending at the air-foil leading edge, normalized by the airfoil chord c. Note that s is negative for impingement locations on the lower side of the airfoil, while it is positive on the upper side. Also, the leading edge of a finite-thickness airfoil is located at $s \equiv 0$, while the trailing edge corresponds to values of $|s| \geq 1$. Results for impact of insect and sand grain are discussed in Sections 4.1 and 4.2 respectively.

4.1. Insect simulation

Insect trajectories and impact properties were evaluated at $r/R = 0.35, 0.65$ and 0.75, corresponding to the airfoils DU 97-W-300, DU 96-W-212, and DU 96-W-180, respectively. The normalized excrescence height ε with respect to insect length l_I, and normalized normal impact velocity V_N with respect to V_∞, are presented in Figs. 3, and 4, respectively, as a function of airfoil arc length s. Peak values of ε are reached in the vicinity of $s = 0$ at all sections. However, for the three cases considered the maximum value of ε is reached at $r/R = 0.75$, where the highest simulated freestream velocity occurs [Fig. 3(c)], while the peak of ε decays steadily when moving to inboard sections, as shown in Figs. 3(b) and 3(a). Changing angle of attack has a modest effect on the peak value of excrescence height. At increased angles of attack, maximum values of ε move slightly toward negative values of s, following the shift in the stagnation streamline. Also, the insect impingement limits move forward on the upper surface and aft on the lower surface with increasing angle of attack. In fact, for $\alpha = 8$ deg the lower impingement limit reaches the trailing edge of the airfoil, as shown in Figs. 3(c) and 4(c).

Normal impact velocity curves, depicted in Fig. 4, show a common behavior throughout the blade span. Velocity at impact increases at a lower rate from the lower impingement limit toward the stagnation streamline compared with the upper impingement limit toward $s = 0$. For all locations, an increment in angle of attack promotes a shallower gradient toward the peak value of V_N/V_∞ on the pressure side ($s < 0$), while the effect is reversed on the suction side of the airfoils ($s > 0$). A maximum value of $V_N/V_\infty = 1.0$ is reached at $r/R = 0.75$, and 0.65 in Figs. 4(b) and 4(c), while the maximum value of V_N/V_∞ is smaller at the most inboard section of the blade, as shown in Fig. 4(a). Moreover, a rounded peak of V_N/V_∞ appears on thick blade sections, characterized by large leading edge radii [Fig. 4(a)], as opposed to thinner sections with smaller leading edge radii [Figs. 4(b) and 4(c)].

Insect impact efficiency, rupture ratio, and quantity of debris are plotted in Fig. 5. The three blade sections are characterized by comparable values of E_I for smaller values of a, as shown in Fig. 5(a).
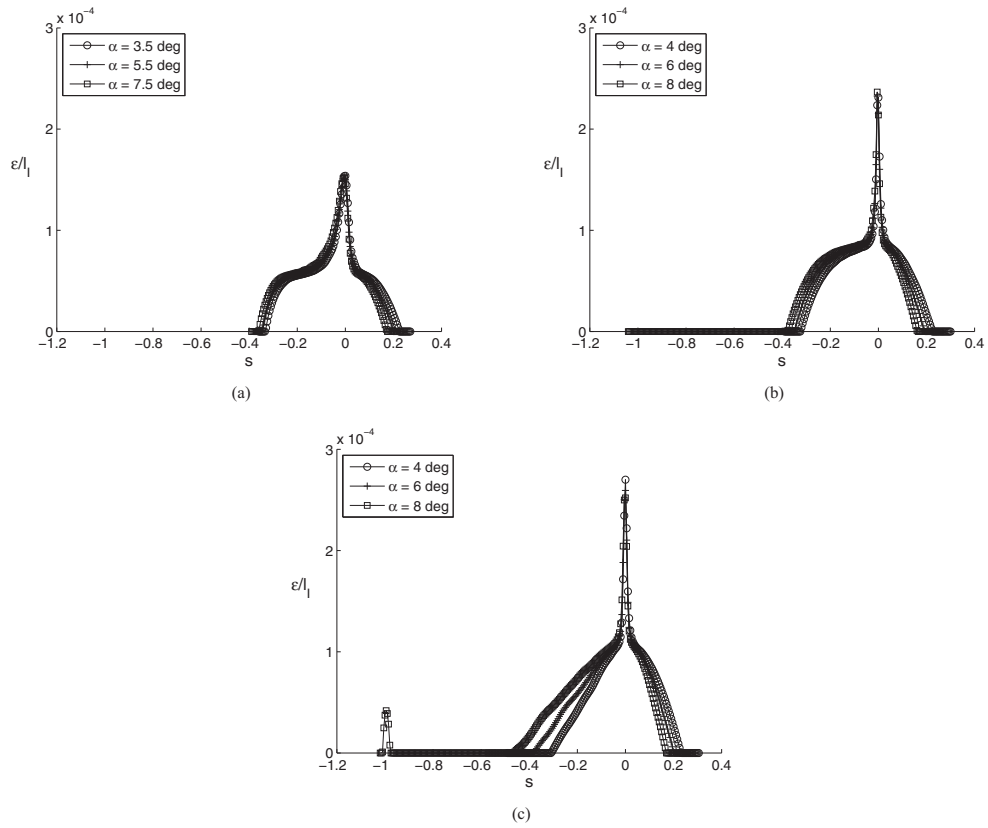
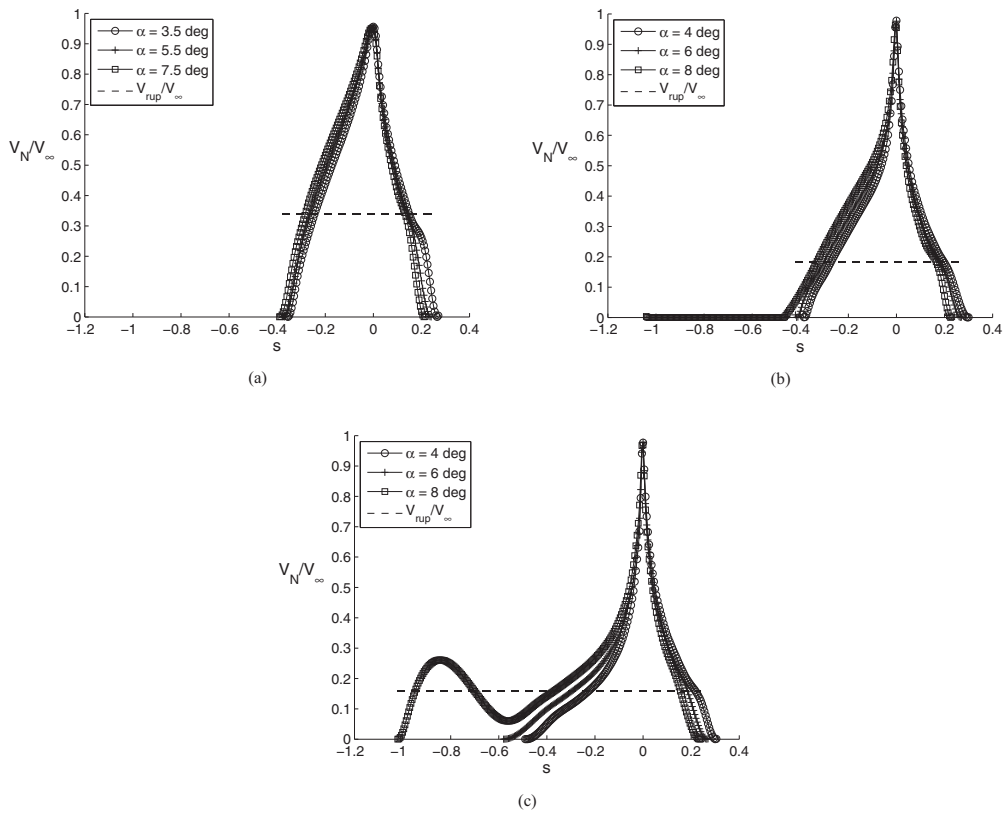Figure 3. Insect ε curves at (a) $r/R = 0.35$, (b) 0.65, and (c) 0.75.

Figure 4. Insect V_N curves at (a) $r/R = 0.35$, (b) 0.65, and (c) 0.75.
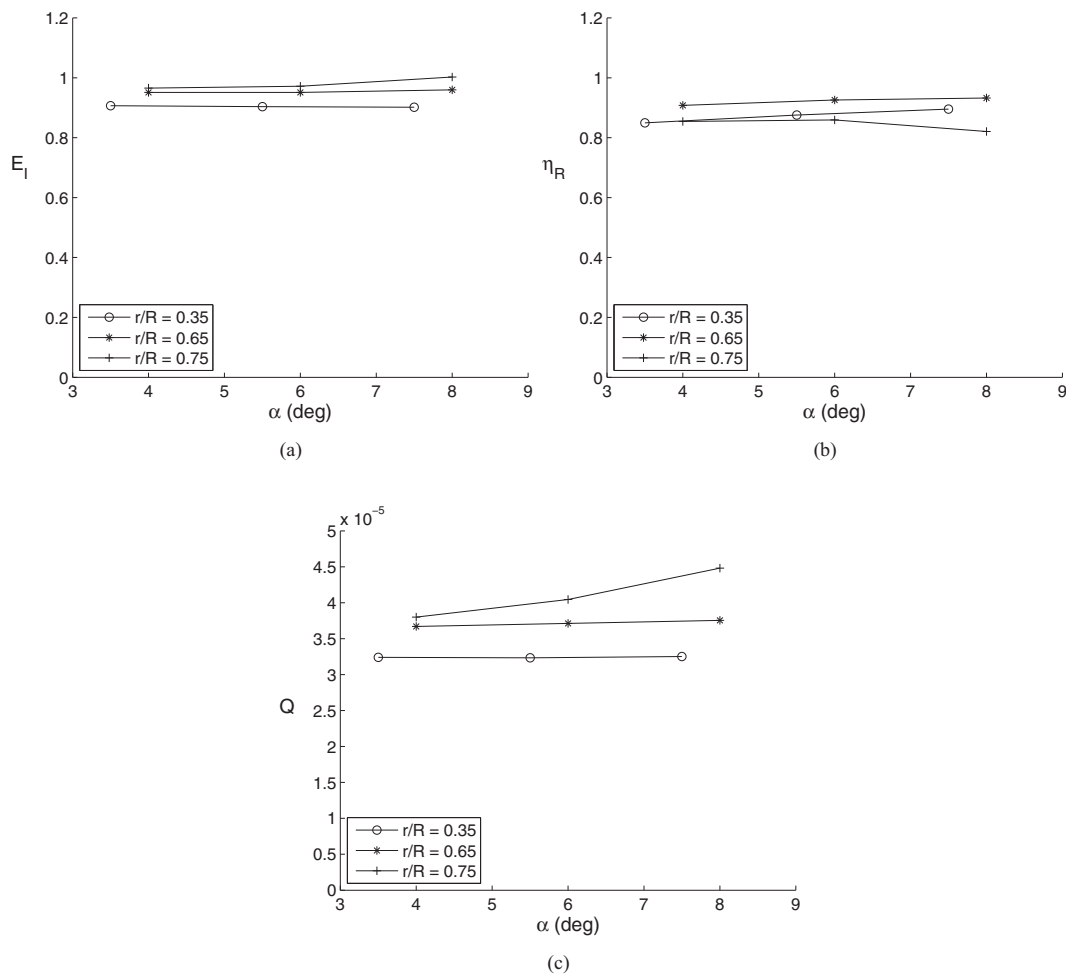
Figure 5. Insect (a) impingement efficiency E_I, (b) rupture ratio η_R, and (c) quantity of debris Q at three blade spanwise locations.

When $\alpha = 8$ deg, the largest value of E_I is observed at the section located at $r/R = 0.75$. Impact efficiency shows a weak correlation with α at all blade sections. Also, Fig. 5(b) shows that rupture ratio η_R is comparable at all three sections for small angles of attack. In general, it is observed that higher impingement efficiencies appear for outboard sections of the blade, while comparable values of rupture efficiencies can be observed at each section, with fair insensitivity to angle of attack.

Figure 5(c) shows the quantity of insect debris Q as a function of α along the blade. The blade section with highest values of Q is located at $r/R = 0.75$, followed by the section at $r/R = 0.65$, and 0.35. In general, Q represents a greater volume of insect debris deposited on the outboard and faster blade sections, compared with the inboard locations. Smaller insect rupture velocity V_{rup}/V_∞ exists at more outboard sections, compared with lower r/R-locations along the blade, as also reflected by higher values of η_R [Fig. 5(b)].

Results for the insect impingement and rupture surface ratio are shown in Fig. 6. The insect impact surface ratio R_I is maximum at the two most outboard sections, where $r/R = 0.65$ and 0.75, as shown in Fig. 6(a). The parameter R_I does not display a strong correlation with lower values of angle of attack; whereas, for values of $\alpha > 6$ deg a jump in R_I is observed at those locations. For thinner blade sections, the jump in R_I is due to the increased exposed area of the blade to impingement at higher values of a, as also shown in Figs. 3(b) and 3(c). The rupture surface ratio R_R is presented in Fig. 6(b). The highest values of R_R appear at $r/R = 0.65$ and 0.75, where freestream velocities are higher. It can be concluded that sections with higher freestream velocities and smaller leading edge radii [Figs. 7(b) and 7(c)] promote insect rupture on a larger portion of the surface area compared with slower and more inboard thicker sections [Fig. 7(a)].
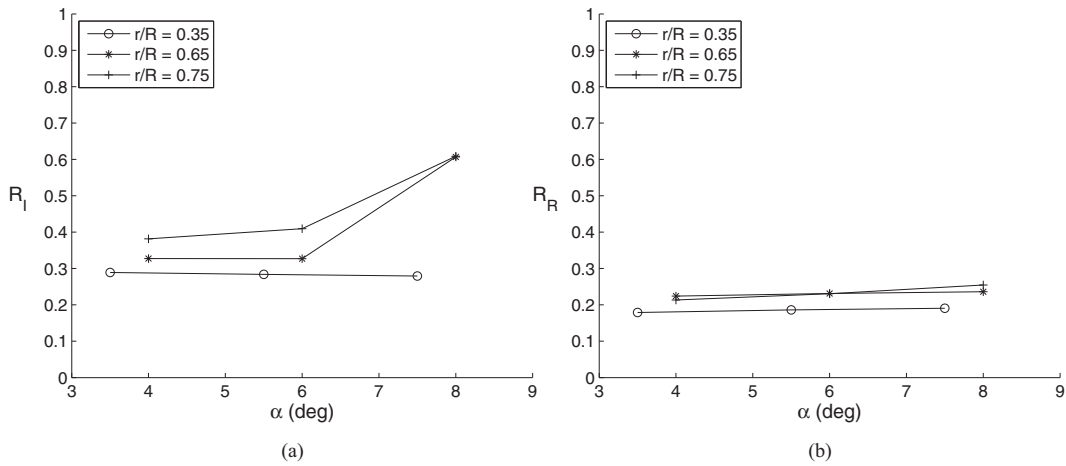
Figure 6. Insect (a) impact surface ratio R_I and (b) rupture surface ratio R_R at three blade spanwise locations
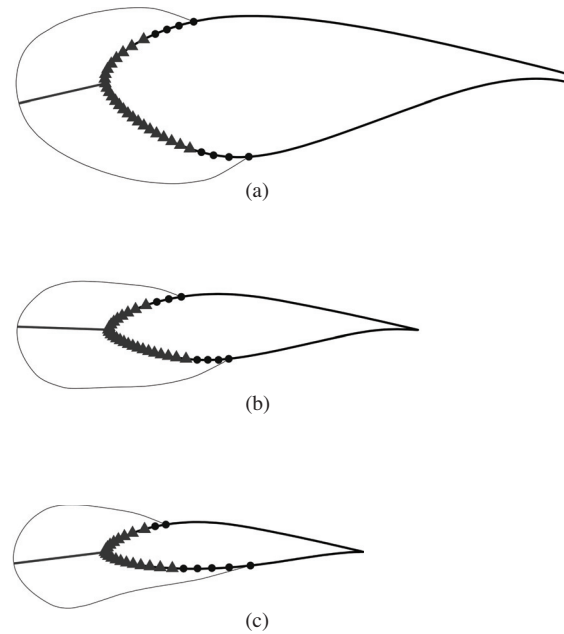

Figure 7. Contours of insect normal impact velocity V_N/V_∞ at (a) $r/R = 0.35$ ($\alpha = 5.5$ deg), (b) $r/R = 0.65$ ($\alpha = 6$ deg), (c) and $r/R = 0.75$ ($\alpha = 6$ deg); circles placed at impingement locations, triangles at rupture locations, straight segments at maximum V_N/V_∞.

4.2. Sand simulation

Three blade sections were simulated for sand erosion, and curves of impingement efficiency β and erosion rate E are plotted versus airfoil arc length s in Figs. 8 and 9. At $r/R = 0.35$ a rounded peak of $\beta \approx 0.9$ appears in the proximity of $s = 0$ for all angles of attack [Fig. 8(a)]. An increment in α causes the sand β-curve to shift toward negative values of s, indicating an increased probability of sand impingement on the pressure side of the airfoil ($s < 0$). Moving toward the blade tip, the peak of β is sharper, and its maximum value is approximately 1.0, as shown in Figs. 8(b) and 8(c). The smaller relative thickness and nose radii of the DU 96-W-212 and −180 airfoils compared with the DU 97-W-300 airfoil yield the increase of β. When airfoil thickness is reduced, β increases in maximum value and in growth gradient along s.

By analyzing the curves for erosion rate E in Fig. 9, a common behavior is apparent for the three blade sections. While there are two peaks, the maximum value of E is reached on the suction side of all airfoils ($s > 0$) at locations slightly aft of the leading edge. At higher angles of attack, the peak
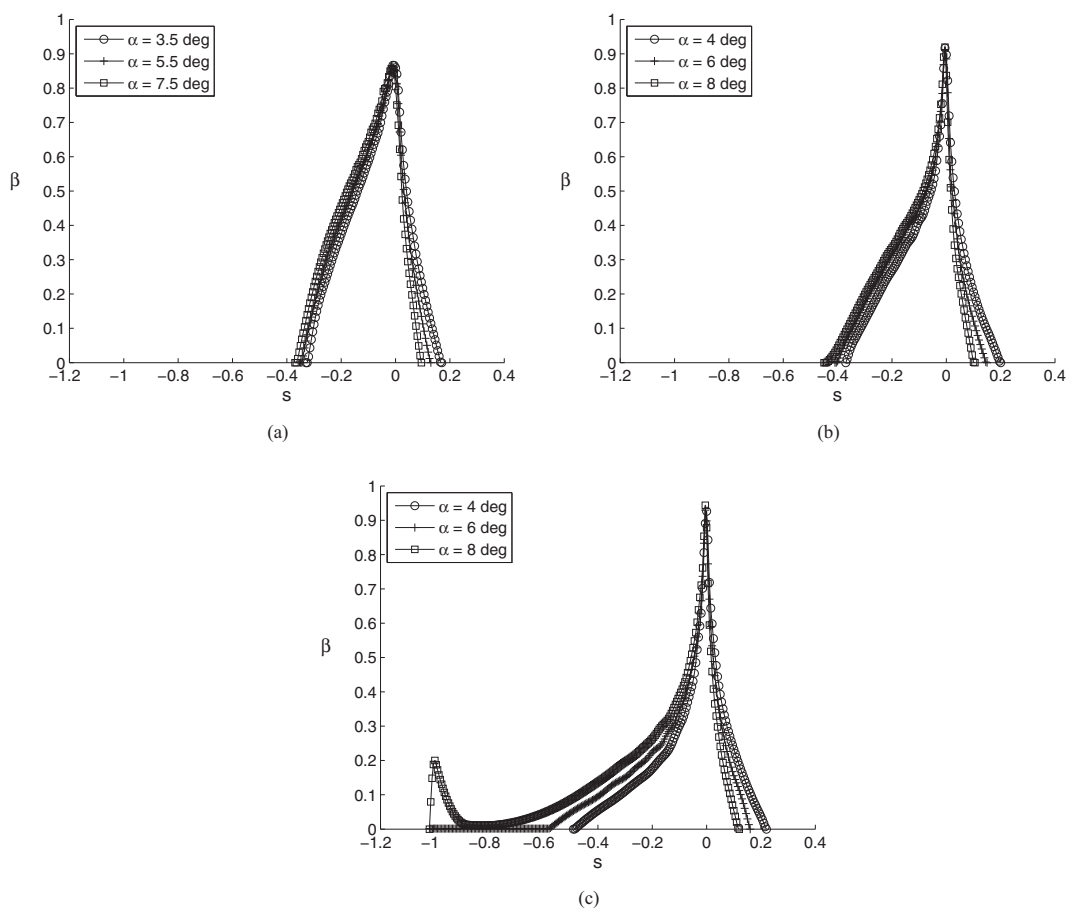
Figure 8. Sand β curves at a r/R of (a) 0.35, (b) 0.65, and (c) 0.75

value of E increases and appears at lower values of s, closer to the leading edge. On the pressure side of the airfoil ($s < 0$), a broader but lower peak of erosion rate is observed. In general, the peak values of erosion rate are consistently lower on the pressure side of all airfoils with respect to the peak values at the suction side.

The values E at the blade leading edge ($s = 0$) are close to zero for all sections. This behavior is physical and intrinsic in the coefficients K and n used to model eqn. (30) (see Table 4). Erosion experiments on flat-plate plastic materials show a peak in erosion rate for impact angles ≈ 30 deg, while two minima are reached for tangent ($\theta = 0$ deg) and normal impacts ($\theta = 90$ deg) [28, 51, 56]. The present erosion simulations reflect a coherent behavior in the proximity of the stagnation line, where $s \approx 0$ and $\theta \approx 90$ deg. When considering sand particles impinging away from such region, their impact velocity is higher while their impact angle is lower, which results in a peak of erosion rate at $\theta \approx 22$ deg. As θ approaches 0 deg, the erosion rate on the blade surface becomes negligible. Finally, the overall blade maximum erosion rate is reached at the most outboard section, located at $r/R = 0.75$ [Fig. 9(c)], while a value of E an order of magnitude lower is observed at $r/R = 0.35$ [Fig. 9(a)]. It can be concluded that given a ratio of freestream velocities $V_{\infty, 0.35}/V_{\infty, 0.75} \approx 0.5$, an erosion rate significantly lower is observed for the more inboard section of the blade.

The impact efficiency E_I is plotted versus angle of attack in Fig. 10(a). As α increases, E_I increases linearly at all three blade locations. The section showing highest values of E_I is the thickest, while the thinnest airfoil shows the lowest values. Sand grains are lighter and smaller than insects, and this fact is reflected by values of E_I being greater than unity for the majority of test cases. An inflection in the sand grain upper limit trajectory exists as the particle approaches the blade section. The trajectory inflection makes values of $E_I > 1$ appear. The smallest envelope of sand grains is captured by the blade sections at $r/R = 0.65$ and 0.75. On the other hand, by analyzing Fig. 10(b), maximum
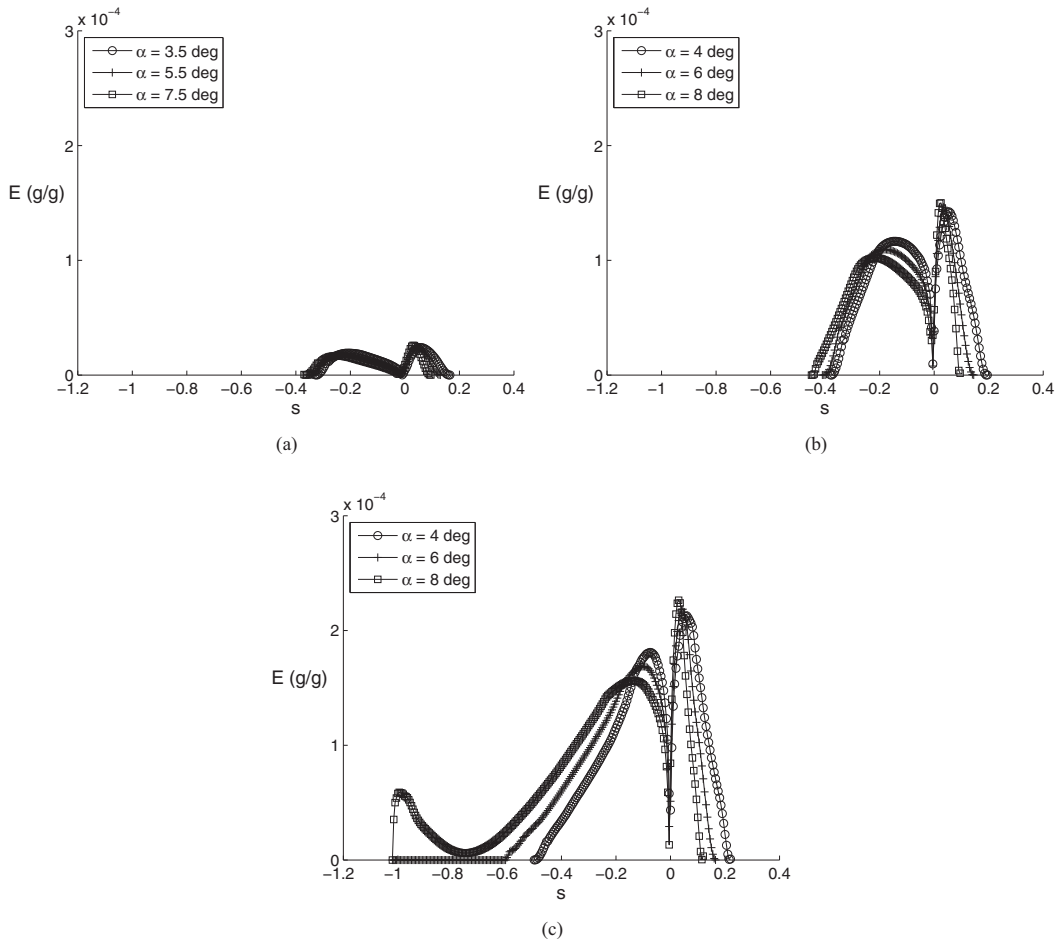
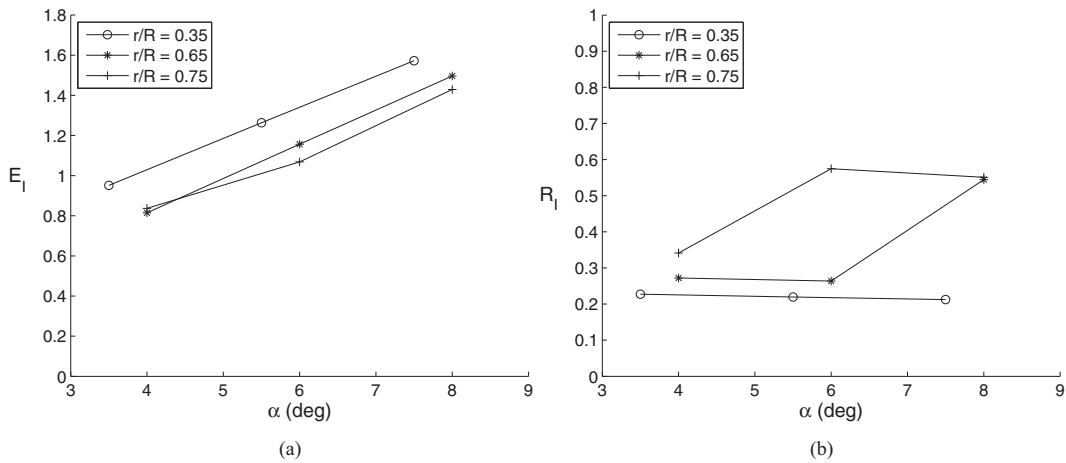Figure 9. Sand E curves at a r/R of (a) 0.35, (b) 0.65, and (c) 0.75

Figure 10. Sand (a) impingement efficiency E_I and (b) impact surface ratio R_I at three blade spanwise locations

impact surface ratio R_I appears at the outboard section, where $r/R = 0.75$. The surface area of sand grains at $r/R = 0.35$ is approximately a third in size compared with $r/R = 0.75$. For $\alpha = 8$ deg, comparable values of R_I appear at $r/R = 0.65$ and 0.75.

To shed more light on the blade erosion characteristics, E versus impact angle θ is plotted for the most inboard section ($r/R = 0.35$) at $\alpha = 3.5$ deg in Fig. 11. The peak of erosion rate occurs
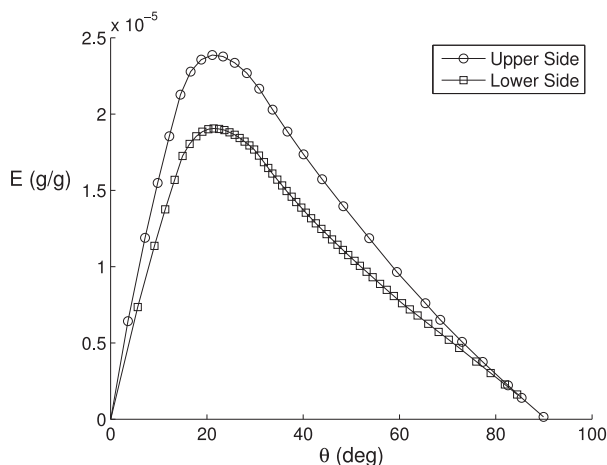
Figure 11. Sand erosion rate E at $r/R = 0.35$ and $\alpha = 3.5$ deg

at $\theta = 22$ deg, for both upper and lower blade sides. The role played by the distribution of impact velocity around the curved surface of the blade is apparent. A larger value of E is observed on the blade upper side where dynamic pressure is higher, as opposed to the blade lower side, where E is lower. Such behavior is correlated to the velocity flowfield around the blade section.

A broader range of negligible erosion rate in the vicinity of the stagnation point is observed at $r/R = 0.35$, as shown in Fig. 12(a), compared with thinner and more outboard sections [see Figs. 12(b) and 12(c)]. On the other hand, a wider range of negligible erosion rate is observed on the blade pressure side at $r/R = 0.75$ [Fig.12(c)] as compared with more inboard sections. When moving toward the blade tip, both of the peaks in E increase in value and move toward the blade leading edge, particularly the pressure side peak.
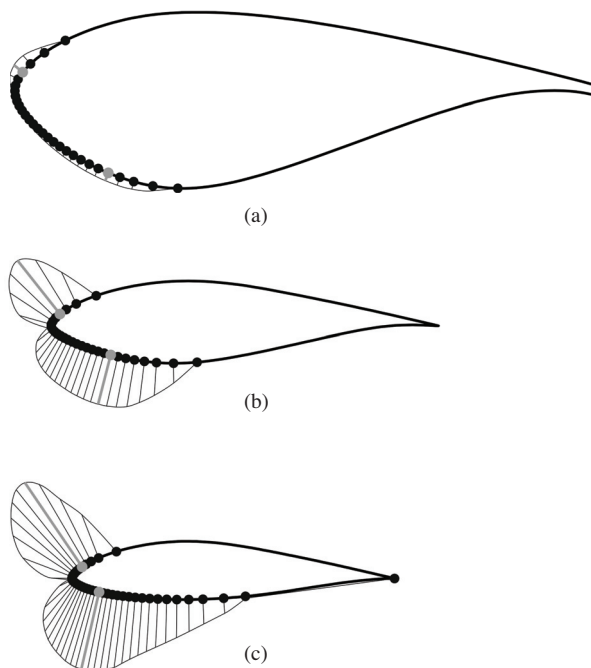

(a)

(b)

(c)

Figure 12. Contours of sand erosion rate E at (a) $r/R = 0.35$ ($\alpha = 5.5$ deg), (b) $r/R = 0.65$ ($\alpha = 6$ deg), and (c) $r/R = 0.75$ ($\alpha = 6$ deg), where the black circles are placed at sand grain impact locations, and the grey circles indicate maximum E on the blade suction and pressure sides

The result of a continuous erosion produced by sand grains may appear as core composite material exposure in the vicinity of the blade leading edge, where E has a maximum. However, the erosion mechanism associated with composite matrix materials used for wind turbine blades [57, 58] typically shows maximum erosion rate for θ in the range of 45–55 deg [59–61]. In general, composite matrix materials have different erosion constants K and n compared with the outer coating.

A proposed model to explain operational damage to blades due to airborne particles is as follows:

1. Particles collide mainly in the proximity of the blade leading edge. The maximum observed insect debris thickness is close to the blade stagnation point; whereas, sand grains collide with the blade surface and promote two erosion peaks downstream of the stagnation point, where impact angles reach ≈ 22 deg.
2. Over the long term, sand erosion may cause a removal of coating material where E is high. On the other hand, a narrow strip of intact coating may be left along the very leading edge of the blade, where the erosion rate is significantly lower [see Fig. 13].
3. The bonding properties of the leading edge residual coating may decay due to a lack of coating integrity. The detachment of this residual coating is further promoted by impact with heavier particles such as insects. A completely uncoated area in the proximity of the leading edge may result as a consequence.
4. The action of sand grains continues by eroding the composite core matrix of the blade. However, the peak of erosion rate for core matrix materials occurs at $\theta \approx 45$– 55 deg [54, 59– 61]. In such conditions, the peak of E shifts to s-locations closer to the stagnation line of the blade, causing further damage at that location.
5. Assuming the absence of cracks in the coating, the erosion proceeds from areas just downstream of the leading edge to more upstream locations. Such behavior is valid when plastic-based coatings and composite core materials are chosen for blade manufacturing.

The results for insect and sand grain impact are summarized in Table 6. Note that the rupture ratio η_R and rupture surface ratio R_R may be defined for insects, but not for sand grains.
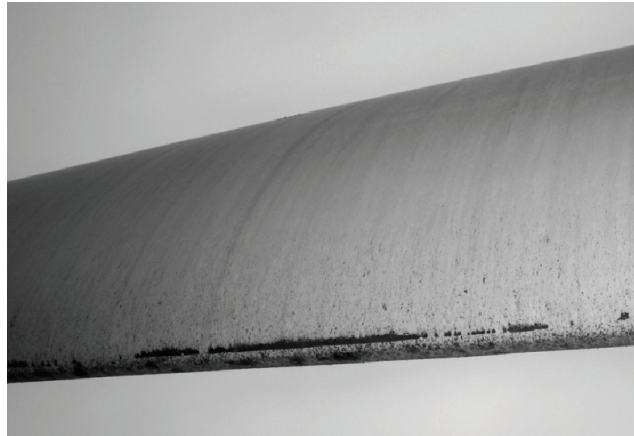

Figure 13. Leading edge of a wind turbine blade exposed to erosion (courtesy of 3M)

Table 6. Average values of impact efficiency, rupture ratio, impact surface ratio, and rupture surface ratio

Particle	r/R	$(E_I)_{avg}$	$(\eta R)_{avg}$	$(R_I)_{avg}$	$(R_R)_{avg}$
	0.35	0.904	0.874	0.284	0.185
Insect	0.65	0.954	0.922	0.420	0.230
	0.75	0.980	0.844	0.466	0.233
	0.35	1.262	–	0.220	–
Sand	0.65	1.156	–	0.360	–
	0.75	1.111	–	0.489	–

5. CONCLUSION

The present paper described simulations to evaluate operational damage of wind turbine blades due to insects and sand grains. The trajectories of impinging particles were evaluated through a numerical code that computed particle properties at impact. The average values of impact efficiency, rupture ratio, impact surface ratio, and rupture surface ratio along the blade were reported. Values of average impact efficiency E_I slightly increase for insects along the span, while they decrease for sand grain collision. Average values of rupture ratio η_R are comparable at all blade sections; however, the highest value appears at $r/R = 0.65$. Another result is given by the average impact surface ratio R_I which increases along the blade for both insects and sand grains, meaning that larger portions of the blade surface are exposed to particle collisions. Larger rupture surface ratio R_R is found at higher freestream velocities and thinner blade sections, meaning that a larger surface area of the blade is exposed to insect rupture at such locations when compared with inboard locations. A similar result is given by the quantity of insect debris Q along the blade, which is also larger at outboard sections.

The erosion analysis showed that two peaks of erosion rate appear at each blade section. A higher erosion rate is reached where freestream velocities are greater. In fact, values of maximum erosion rate approximately ten times higher occur at $r/R = 0.75$ compared with the most inboard section, $r/R = 0.35$ due to the nonlinear behavior of erosion rate through sand impact velocity. This conclusion is remarkable, considering a freestream velocity approximately 50% lower at $r/R = 0.35$, compared with the freestream velocity at $r/R = 0.75$. Also, it was observed that a higher erosion rate occurs on the blade suction side, while a lower peak appears on the pressure side for the considered angles of attack. Conversely, the blade upper surface shows narrower ranges of higher erosion rate compared with lower but broader ranges on the bottom surface. When moving toward the blade tip, the two peaks of erosion rate come closer and approach the blade leading edge. In an actual case with photo record, it was observed that the first visible erosion damage would appear at such locations.

REFERENCES

[1] Dalili, N., Edrisy, A. and Carriveau, R. 2007. "A Review of Surface Engineering Issues Critical to Wind Turbine Performance". *Renewable and Sustainable Energy Reviews*, 13, pp. 428–438.

[2] Hayman, B., Wedel-Heinen, J. and Brondsted, P. 2008. "Materials Challenges in Present and Future Wind Energy". *MRS Bulletin*, 33, Apr., pp. 343–353.

[3] Singh, S., Bhatti, T. S. and Kothari, D. P. 2012. "A Review of Wind-Resource-Assessment Technology". Centre for Energy Studies, Indian Institute of Technology. Hauz Khas, New Delhi 110016.

[4] Huang, C. W., Yang, K., Liu, Q., Zhang, L., Bai, J. Y. and Xu, J. Z. 2011. "A Study on Performance Influences of Airfoil Aerodynamic Parameters and Evalutation Indicators for the Roughness Sensitivity on Wind Turbine Blade". *Science China - Technological Sciences*, 54(11), pp. 2993–2998.

[5] Siochi, E. J., Eiss, N. S., Gilliam, D. R. and Wightman, J. P. 1987. "A Fundamental Study of the Sticking of Insect Residues to Aircraft Wings". *Journal of Colloid and Interface Science*, 115(2), pp. 346–356.

[6] Croom, C. and Holmes, B. 1986. "Insect Contamination Protection for Laminar Flow Surfaces". NASA Langley Research Center, N88-14954/7, Hampton, VA, Dec.

[7] Carmichael, B. H. 1979. "Summary of Past Experience in Natural Laminar Flow and Experimental Program for Resilient Trailing Edge". Low Energy Transportation Systems, Capistrano Beach, CA 92624, for Ames Research Center, NASA CR 152276, May.

[8] Shankar, P. 2001. "Can Insects Seriously Affect the Power Output of Wind Turbines?". *Current Science*, 81(7), pp. 747–748.

[9] Corten, G. P. and Veldkamp, H. F. 2001. "Insects can Halve Wind-Turbine Power". *Nature*, 412, pp. 41–42.

[10] Ragheb, A. and Selig, M. S. 2011. "Multi-Element Airfoil Configurations for Wind Turbines". In Proceedings of the 29th AIAA Conference, AIAA Paper 2011–3971.

[11] Schneiderhan, T., Schulz-Stellenfleth, J., Lehner, S. and Hortsmann, J. 2002. "Sar Wind Fields for Off-shore Wind Farming". DLR, Oberpfaffenhofen, 82230 Wessling, Germany.

[12] DNV, 2010. "Design and Manufacture of Wind Turbine Blades, Offshore and Onshore Wind Turbines - October 2010". Standard DNV-DS-J102, Det Norske Veritas, Oct.

[13] Arrighetti, C., Pratti, G. D. and Ruscitti, R. 2003. "Performance Decay Analysis of New Rotor Blade Profiles for Wind Turbines Operating in Offshore Environments". *Wind Engineering*, 27(5), pp. 371–380.

[14] Khakpour, Y., Bardakji, S. and Nair, S. 2007. "Aerodynamic Performance of Wind Turbine Blades in Dusty Environments". In International Mechanical Engineering Congress and Exposition, Seattle, Washington, IMECE2007–43291.

[15] Tilly, G. 1969. "Erosion Caused by Airborne Particles". *Wear*, 14(1), pp. 63–79.

[16] Davis, J. R., ed., 2001. *Surface Engineering for Corrosion and Wear Resistance*. ASM International - The Materials Information Society. 10M Communications, Materials Park, OH 44073-0002, ch. 3, pp. 43–86.

[17] Wood, R. J. K. 1999. "The Sand Erosion Performance of Coatings". *Materials and Design*, 20(4), pp. 179–191.

[18] Tabakoff, W. and Balan, C. 1983. "A Study of the Surface Deterioration due to Erosion". *Presented at the 28th ASME Interational Gas Turbine Conference and Exhibit, Phoenix, Arizona*, 105, pp. 834–838.

[19] Rempel, L. 2012. "Rotor Blade Leading Edge Erosion - Real Life Experiences". Oct. URL http://www.windsytemsmag.com.

[20] Sareen, A., Sapre, C. A. and Selig, M. S. 2012. "Effects of Leading-Edge Protection Tape on Wind Turbine Blade Performance". *Wind Engineering,* 36(5), pp. 525–534.

[21] Hayman, B., 2007. "Approaches to Damage Assessment and Damage Tolerance for FRP Sandwich Structures". *Journal of Sandwich Structures and Materials*, 9, pp. 571–596.

[22] Ragheb, A. M. and Ragheb, M. 2011. "Wind Turbine Gearbox Technologies". In *Fundamental and Advanced Topics in Wind Power*, R. Carriveau, ed. In-Tech, pp. 189–206.

[23] Ciang, C. C., Lee, J. R. and Bang, H. J. 2008. "Structural Health Monitoring for a Wind Turbine System: a Review of Damage Detection Methods". *Measurement Science and Technology*, 19(12), Oct., pp. 122001–122021.

[24] Soltani, M. R., Birjandi, A. H. and Seddighi-Moorani, M. 2011. "Effect of Surface Contamination on the Performance of a Section of a Wind Turbine Blade". *Scientia Iranica B*, 18(3), pp. 349–357.

[25] Mayor, G. S., Moreira, A. B. B. and Munoz, H. C. 2013. "Influence of Roughness in Protective Strips of Leading Edge for Generating Wind Profiles". In 22nd International Congress of Mechanical Engineering, COBEM 2013.

[26] Ren, N. and Ou, J. 2009. "Dust Effect on the Performance of Wind Turbine Airfoils". *Journal of Electromagnetic Analysis and Applications*, 1(2), pp. 102–107.

[27] Romero-Sanz, I. and Matesanz, A., 2008. "Noise Management on Modern Wind Turbines". *Wind Engineering*, 32(1), pp. 27–44.

[28] Arjula, S. and Harsha, A. P. 2006. "Study of Erosion Efficiency of Polymers and Polymer Composites". *Polymer Testing*, 25(2), pp. 188–196.

[29] Challener, C. 2010. "coatings critical for wind energy efficiency". JCT CoatingsTech, Jan.

[30] Ragheb, M. 2010. "USA Wind Energy Resources". University of Illinois at Urbana-Champaign, NPRE 475 lecture notes, Urbana, IL 61801, Jan.

[31] Bragg, M. B. and Maresh, J. L., 1986. A Numerical Method To Predict The Effect of Insect Contamination on Airfoil Drag. Aeronautical and Astronautical Engineering Report AARL 86-01, The Ohio State University Research Foundation, OH 43212, Mar.

[32]   Drela, M. 1989. "XFOIL: An Analysis and Design System for Low Reynolds Number Airfoils". In *Low Reynolds Number Aerodynamics*, T. J. Mueller, ed., Vol. 54 of *Lecture Notes in Engineering*. Springer-Verlag, New York, June, pp. 1–12.

[33]   Roskam, J. 1995. *Airplane Flight Dynamics and Automatic Flight Controls*. DARcorp, Lawrence, KS 66044.

[34]   Bragg, M. B. 1982. "Rime Ice Accretion and Its Effect on Airfoil Performance". NASA Lewis Research Center, NASA CR-165599, Mar.

[35]   Langmuir, I. and Blodgett, K. 1946. Mathematical Investigation of Water Droplet Trajectories. Tech. Rept. 5418, U.S. Army Air Force.

[36]   Hamed, A. A., Tabakoff, W., Rivir, R. B., Das, K. and Arora, P. 2005. "Turbine Blade Surface Deterioration by Erosion". *Journal of Turbomachinery*, 127(3), pp. 445–452.

[37]   Wilson, R. E. 2009. "Wind Turbine Aerodynamics Part A: Basic Principles". In *Wind Turbine Technology, Fundamental Concepts of Wind Turbine Engineering*, *Second Edition*, D. A. Spera, ed. ASME Press, Three Park Avenue, New York City, NY 10016, pp. 281–350.

[38]   Timmer, W. A. and van Rooij, R. P. J. O. M. 2003. "Summary of the Delft University Wind Turbine Dedicated Airfoils". *Journal of Solar Energy Engineering*, 125(4), pp. 571–596.

[39]   Freeman, J. 1945. "Studies in the Distribution of Insects by Aerial Currents". *Journal of Animal Ecology,* 14(2), pp. 128–154.

[40]   Nachtigall, W. 1974. *Insects in Flight*. HarperCollins Publishers LLC, New York.

[41]   Vogel, S., 1967. "Flight in Drosophila, III, Aerodynamic Characteristics of Fly Wings and Wing Models". *Journal of Experimental Biology*, 46, pp. 431–443.

[42]   Sun, M. and Wu, J. H. 2003. "Aerodynamic Force Generation and Power Requirements in Forward Flight in a Fruit Fly with Modeled Wing Motion". *The Journal of Experimental Biology*, 206(17), pp. 3065–3083.

[43]   Hoerner, S. F. 1965. *Fluid-Dynamic Drag*. Hoerner Fluid Dynamics, Bakersfield, CA 93390.

[44]   Nachtigall, W. 2001. "Some Aspects of Reynolds Number Effects in Animals". *Mathematical Methods in the Applied Sciences*, 24, pp. 1401–1408.

[45]   Lehmann, F. O. 2002. "The Constraints of Body Size on Aerodynamics and Energetics in Flying Fruit Flies: An Integrative View". *Zoology*, 105(4), pp. 287–295.

[46]   Haider, A. and Levenspiel, O. 1989. "Drag Coefficient and Terminal Velocity of Spherical and Nonspherical Particles". *Powder Technology*, 58(1), pp. 63–70.

[47]   Coleman, W. S. 1961. "Roughness Due to Insects". In *Boundary Layer and Flow Control*, G. V. Lachmann, ed., Vol. 2. Pergamon Press, pp. 682–747.

[48]   Feuerstein, A. and Kleyman, A. 2009. "Ti-N Multilayer Systems for Compressor Airfoil Sand Erosion Protection". *Surface and Coatings Technology*, 204(6–7), pp. 1092–1096.

[49]   Maozhong, Y., Baiyun, H. and Jiawen, H. 2002. "Erosion Wear Behaviour and Model of Abradable Seal Coating". *Wear*, 252(1–2), pp. 9–15.

[50]   Wood, K. 2011. "Blade Repair: Closing the Maintenance Gap," Composites World, Apr. URL http://www.compositesworld.com.

[51]   Zahavi, J. and Jr., G. F. S. 1981. "Solid Particle Erosion of Polymeric Coatings". *Wear*, 71(2), pp. 191–210.

[52]   Arjula, S., Harsha, A. P. and Ghosh, M. K. 2008. "Solid-particle Erosion Behavior of High-Performance Thermoplastic Polymers". *Journal of Material Science,* 43(6), pp. 1757–1768.

[53]   Harsha, A. P. and Thakre, A. A. 2007. "Investigation on Solid Particle Erosion Behaviour of Polyetherimide and its Composites". *Wear*, 262(7–8), pp. 807–818.

[54]   Barkoula, N.-M. and Karger-Kocsis, J. 2002. "Review – Processes and Influencing Parameters of the Solid Particle Erosion of Polymers and Their Composites". *Journal of Materials Science*, 37, pp. 3807–3820.

[55]   Drela, M. 2014. *Flight Vehicle Aerodynamics*. The MIT Press, Cambridge, Massachusetts – London, England.

[56]   Kharde, Y. R. and Saisrinadh, K. V. 2008. "Effect of Particle Velocity, Temperature and Impingement Angle on the Erosive Wear Behavior of Polymer Matrix Composites". *International Journal of Applied Engineering Research*, 12, pp. 1689–1695.

[57]   Tangler, J. L. 2000. "The Evolution of Rotor and Blade Design". In Presented at the American Wind Energy Association, Wind Power 2000, NREL CP-500-28410.

[58]   Thomsen, O. T. 2009. "Sandwich Materials for Wind Turbine Blades - Present and Future". *Journal of Sandwich Structures and Materials*, 11(7), pp. 7–26.

[59]   Ahmed, T. J. Ninho, G. F., Bersee, H. E. N. and Beukers, A., 2009. "Improving Erosion Resistance of Polymer Reinforced Composites". *Journal of Thermoplastic Composite Materials*, 22, pp. 703–725.

[60]   Drensky, G., Hamed, A., Tabakoff, W. and Abot, J. 2011. "Experimental Investigation of Polymer Matrix Reinforced Composite Erosion Characteristics". *Wear*, 270(3–4), pp. 146–151.

[61]   Biswas, S. and Satapathy, A. 2009. "Erosion Wear Behavior of Polymer Composites: a Review". *Journal of Reinforced Plastics and Composites*, 29, pp. 2898–2924.